Nanoscale

PAPER

View Article Online
View Journal | View Issue



Cite this: *Nanoscale*, 2025, **17**, 12204

# Engineering biocompatible hydrogen titanate nanocarriers with blood brain barrier (BBB) crossing potential for doxorubicin delivery to glioma cells†

Samraggi Choudhury, ‡[a] Ghrutanjali Sahu,‡[b,c] Pankaj Kharra,[a] Himanshu Sekhar Panda,[a] Laxmidhar Besra,[b,c] Sriparna Chatterjee*[b] and Jiban Jyoti Panda *[a]

$H_2Ti_3O_7$ nanotubes are investigated as promising biocompatible and effective drug delivery systems for cancer therapy. These nanotubes demonstrated high drug encapsulation efficiency of up to 67% for the doxorubicin (Dox) chemotherapeutic agent, translating into a significant drug loading capacity of about 33%. *In vitro* studies demonstrated the successful BBB permeabilizing ability of these nanotubes. The Dox-loaded nanotubes further demonstrated their concentration-dependent cancer cell-killing ability, indicating their adeptness to induce cytotoxicity, DNA degradation and inhibit tumor growth. In addition, assays revealed their ability to generate reactive oxygen species (ROS), particularly hydroxyl radicals, which enhanced the anticancer mechanisms of the Dox-loaded nanotubes. These findings underscore the multifunctionality of $H_2Ti_3O_7$ nanotubes in efficiently delivering chemotherapeutic drugs and generating ROS, making them a promising nanomedicine for targeted cancer therapy. Further detailed *in vitro* and *in vivo* studies are needed to fully understand their anticancer potential and safety profile.

Received 10th January 2025,
Accepted 6th April 2025

DOI: 10.1039/d5nr00126a

rsc.li/nanoscale



## 1. Introduction

One-dimensional (1-D) nanostructures can be described as elongated compositions, which mostly have their diameter in the nanometre range. These 1-D nanostructures comprise nanowires, nanorods, nanotubes, and self-assembled structures. Out of all these structures, nanotubes have gained significant attention in drug delivery because of their unique physicochemical properties like high surface-to-volume ratio, ease of functionalization, *etc*. Loading of therapeutic entities onto or into nanotube systems occurs through steps like adsorption, encapsulation, bonding, *etc*. Controlled release of such loaded moieties, however, depends on the surface properties and morphology of the carrier nanotube. Nanotube-based drug delivery systems often respond to external stimuli such as light, temperature, and pH, which facilitate the demand-specific release of drugs at specific locations within the body. It should be kept in mind that in designing an effective nano-drug delivery system for therapeutic use, the system must be engineered to be biocompatible to reduce potential toxicity concerns. Several ongoing research efforts have been focused on the optimization of the designed synthesis of nanotubes to harness their full potential in the field of drug delivery and attempting to address challenges such as biocompatibility, toxicity, large-scale production, *etc*.[1]

Within the family of one-dimensional nanostructures, carbon nanotubes (CNTs) have emerged as one of the most promising alternatives and efficient tools for transporting therapeutic entities as they can be functionalized with bioactive molecules and can efficiently deliver the cargo to specific cells and organs.[2–4] In nanomedicine, other than CNTs, nanostructures of semiconducting materials with unique physical and chemical properties have also been explored because of their high selectivity and stability. Titanium dioxide ($TiO_2$) is one such semiconducting material that has shown its versatile application in localized drug delivery. Most titania nanotubes, fabricated by anodic oxidation of titanium substrates, are used as drug carriers.[5] However, the anodization process is tricky, and translation to a commercial scale is challenging. This opens up the possibility of exploring

[a]*Institute of Nano Science and Technology, Mohali-140306, Punjab, India. E-mail: jyoti@inst.ac.in*
[b]*Materials Chemistry and Interfacial Engineering Department, CSIR-Institute of Minerals and Materials Technology, Acharya Vihar, Bhubaneswar-751013, Odisha, India. E-mail: sriparna@immt.res.in*
[c]*Academy of Scientific and Innovative Research (AcSIR), Ghaziabad-201002, India*
†Electronic supplementary information (ESI) available. See DOI: https://doi.org/10.1039/d5nr00126a
‡These authors contributed equally to this work.

one of its polymorphs, hydrogen titanate ($H_2Ti_3O_7$), for various applications.

Hydrogen titanate nanostructures are a class of one-dimensional (1D) materials composed of titanium, oxygen, and hydrogen atoms. These nanostructures can take various forms, such as nanotubes, nanowires, and nanobelts, with diameters ranging from a few to hundreds of nanometres and lengths up to several micrometres. Their unique 1D morphology provides a high surface area-to-volume ratio, which is beneficial for applications such as drug delivery, catalysis, and energy storage. Hydrogen titanate nanostructures are typically synthesized using hydrothermal methods, where titanium-based precursors are treated under high temperature and pressure conditions in the presence of a base, such as sodium hydroxide. The resulting sodium titanate nanostructures can then be converted to hydrogen titanate by acid treatment, which replaces the sodium ions with protons. The protons in hydrogen titanate nanostructures can participate in hydrogen bonding interactions, contributing to their stability and potential for functionalization. These unique properties make hydrogen titanate nanostructures promising candidates for various applications, particularly in the field of drug delivery, where their large surface area and tunable properties can be exploited for efficient drug loading and targeted release.

Hydrogen titanate was first synthesized by Kasuga *et al.* in 1998 [5] and since then hydrogen titanate has been explored for its application potential in the fields of catalysis,[6] solar energy,[7] field emitters,[8] ion exchange,[9] supercapacitors,[10] battery materials,[11] gas storage,[12] *etc*. Interestingly, only a handful of studies have been focused on hydrogen titanate as a drug delivery carrier. Ray *et al.* reported the formation of a nano-bioconjugate between $H_2Ti_3O_7$ nanotubes and the vital respiratory protein, cytochrome c.[13] Ranjous *et al.* compared the physicochemical properties of hydrogen titanate with carbon nanotubes and suggested that the titanate could be a promising material for drug delivery because of its appealing properties such as processability, wettability, and biocompatibility.[14] $H_2Ti_3O_7$ nanotubes are strongly hydrophilic[15] in nature and hence are expected to show no or minimum accumulation in the human body, which in turn causes less toxicity in the body.[16] The presence of surface hydroxyl (–OH) groups allows direct conjugation of drugs with the nanostructures for the efficient transport of those drugs.

Numerous hydrophilic anticancer medications are currently employed for therapeutic applications, with doxorubicin (Dox) being recognized as a prominently utilized agent among them.[17] Dox has numerous modes of action, out of which its principal mechanism is the intercalation in the DNA strand. It destabilizes DNA structures and causes strand breakages and damage. Furthermore, this drug has a high capacity to inhibit topoisomerase II, an enzyme required for DNA replication and cell division in cancer cells.[18] Dox has been demonstrated to contribute to breaking DNA double-strands and generating ROS, which leads to apoptosis, senescence, autophagy, and immunomodulatory functions in a cancerous environment.[19]

In this study, we successfully loaded Dox onto $H_2Ti_3O_7$ nanotubes through hydrogen bonding interactions, and the efficacy of this drug delivery system in permeabilizing the BBB against glioblastoma was investigated and reported (Scheme 1).

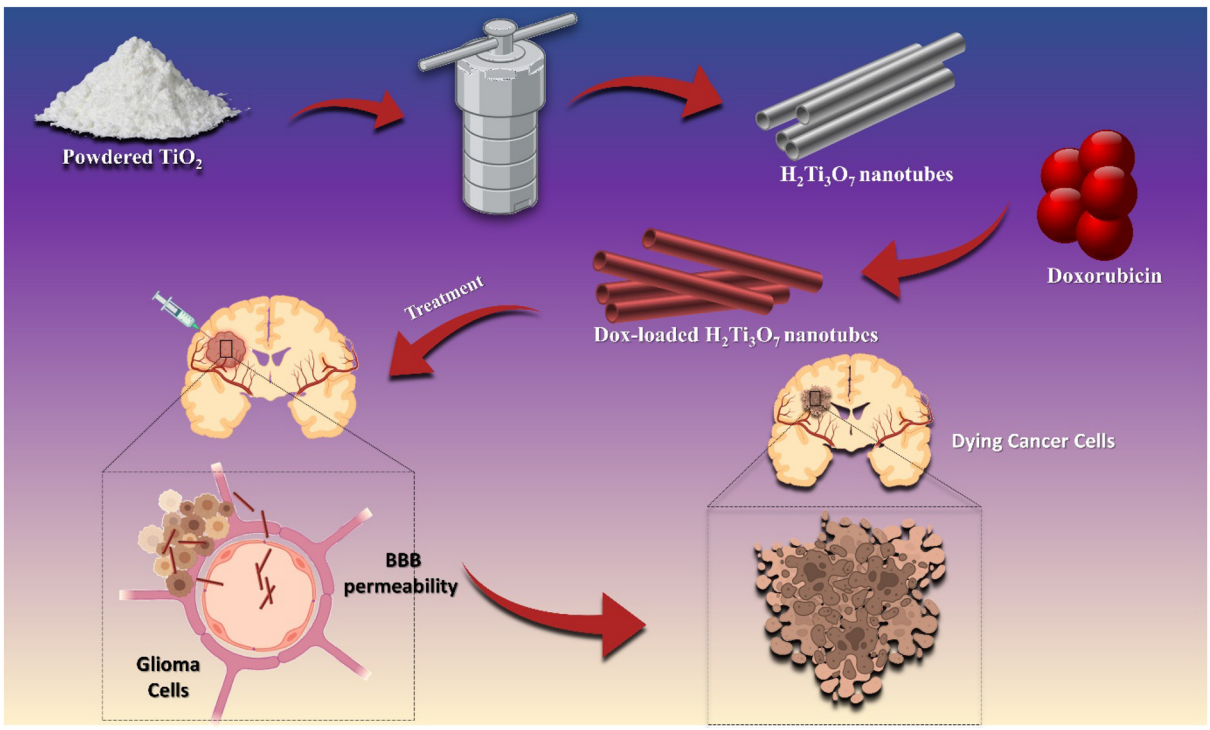


**Scheme 1** Schematic illustration of $H_2Ti_3O_7$ nanotube synthesis and Dox loading for targeted anti-glioma therapy applications. (Created in BioRender. Choudhury, S. (2025) https:// BioRender.com/e3j13qm).

## 2. Experimental details

### 2.1. Synthesis of $H_2Ti_3O_7$ nanotubes

In a typical synthesis procedure, 1 g of commercially available $TiO_2$ (Sigma-Aldrich, 99% purity) was added to an aqueous solution of 10 M NaOH. The mixture was stirred for 30 hours to ensure homogenization and then transferred to a Teflon-lined vessel, which was subsequently autoclaved at 150 °C for 16 hours. After cooling to room temperature, the product was collected by filtration. During filtration, the resulting white powder was thoroughly washed with dilute HCl (prepared by mixing 1 mL of concentrated HCl with 20 mL of deionized water) until the pH of the filtrate reached neutral. Finally, the washed powder was dried in ambient air for 24 hours.

### 2.2 Characterization of $H_2Ti_3O_7$ nanotubes

Crystallographic details of nanostructures in their of the as-prepared state was obtained with a Rigaku Ultima IV (Japan) X-ray diffractometer using Cu Kα radiation of $\lambda$ = 0.154 nm over a $2\theta$ range of 10°–90°. Morphological characterization was performed using a Zeiss Supra field emission scanning electron microscope (FESEM). The details of morphology and structure were further studied using a Tecnai G2 20 Twin FEI transmission electron microscope (TEM). 1 mg of powder sample was dispersed in ethanol by vigorous ultrasonication and 1 drop of suspension was placed on a carbon-coated copper grid for TEM measurement. UV-visible absorption spectra of the prepared powder were recorded in diffuse reflectance mode with $BaSO_4$ as reference using a Shimadzu UV 2450 spectrophotometer. Fourier transform infrared spectra were obtained from 400–4000 $cm^{-1}$ (Thermo Scientific Nicolet iS20 Smart iTX-Diamond ATR-IR spectrometer). The Brunauer–Emmett–Teller (BET) surface area, pore volume, and pore size distribution were obtained from the physisorption of nitrogen at 77 K using a Microtrac BELSORP MINI X surface analyzer. Approximately 100 mg of sample was degassed at 4.5 kPa and 100 °C before nitrogen adsorption. Raman spectroscopy measurements were carried out using a Jobin Yvon T64000 micro-Raman spectrometer.

### 2.3 Cellular biocompatibility assay of $H_2Ti_3O_7$ nanotubes

The biocompatibility of the $H_2Ti_3O_7$ nanotubes was assessed using a mouse fibroblast cell line (L929) by incubating the cells with the nanotubes for 24 hours to evaluate their impact on the cells. The cell viability assay involves adding MTT (3-[4,5-dimethylthiazol-2-yl]-2,5-diphenyl tetrazolium bromide) reagent to the cells and measuring their absorbance signal at a wavelength of 570 nm generated based on the conversion of MTT to formazan crystals by metabolically active cells. The assay is sensitive to changes in cell viability and can detect cytotoxicity induced by the nanotubes.

Immortalized L929 (mouse fibroblast) and C6 (rat glioma) cell lines were acquired from the National Centre for Cell Science (NCCS) Pune. The cells were incubated in Dulbecco's Minimal Essential Medium (DMEM) containing with fetal bovine serum (FBS) and antibiotics (penicillin and streptomycin) in a humidified incubator at 37 °C under 5% $CO_2$.

### 2.4 Dox loading onto $H_2Ti_3O_7$ nanotubes and characterization

The powdered $H_2Ti_3O_7$ nanotubes were dispersed in double-distilled water, followed by probe sonication at 30 A for 30 minutes to obtain a well-dispersed white solution. Then equivalent concentrations of Dox were added to the nanotubes. The drug was permitted to interact with the nanotubes for 96 hours *via* physisorption, and the drug loading percentage was then determined. The drug-loaded nanotubes were further characterized using XPS, FESEM, TEM, FTIR, Raman, and UV techniques.

### 2.5 Drug release kinetics of Dox-loaded $H_2Ti_3O_7$ (Dox-$H_2Ti_3O_7$) nanotubes

To establish a standard curve for Dox, a series of dilutions were prepared by serially diluting 1 mg $mL^{-1}$ Dox solution. The optical density of each dilution was then measured at a wavelength of 485 nm using a multimode plate reader (MPlex Pro 200, Tecan Ltd). The resulting absorbance values were plotted against the corresponding Dox concentrations to generate a concentration *versus* absorbance graph. 1 mg of free Dox and an equivalent amount of Dox loaded onto $H_2Ti_3O_7$ nanotubes were introduced into separate dialysis tubes with a molecular weight cut-off of 6 kDa. These tubes were then immersed in phosphate-buffered saline (PBS) at pH 7.4, and the system was maintained at 37 °C with continuous stirring. The concentration of released Dox was quantified at specific time intervals using a multimode plate reader (MPlex Pro 200, Tecan Ltd). The percentage of the drug released was calculated by dividing the concentration of the released drug by the initial drug concentration. This experimental setup allowed for the evaluation of the release kinetics of Dox from both the free-form and Dox-loaded $H_2Ti_3O_7$ nanotubes, providing insights into their drug release profiles under physiological conditions.[20]

### 2.6 Cellular uptake of Dox-$H_2Ti_3O_7$ nanotubes

The internalization of Dox and Dox-$H_2Ti_3O_7$ nanotubes into C6 cells was investigated using confocal laser scanning microscopy (CLSM-880 with AiryScan, Zeiss). C6 glioblastoma cells were cultured for 24 hours in a 6-well plate with a density of $1 \times 10^5$ cells per well on coverslips. Afterwards, the cells were treated with Dox and Dox-$H_2Ti_3O_7$ at equivalent concentrations. Following an incubation period of 6 hours, the treatment medium was discarded, and the cells were rinsed three times with PBS. The cells were fixed using 4% paraformaldehyde for 15 minutes before being examined under the microscope. This experimental setup allowed for the visualization and comparison of the uptake efficiency of Dox and Dox-$H_2Ti_3O_7$ by the C6 cells, providing insights into the potential benefits of using nanotubes as potential drug delivery vehicles.[21]

### 2.7 Cellular toxicity assay (MTT assay)

To evaluate the cellular toxicity caused by the Dox-$H_2Ti_3O_7$ nanotubes, the cellular viability of C6 cells was determined in

 

the presence of the nanotubes. C6 cells were seeded onto a 96-well plate and, after reaching up to 70% confluency, these cells were treated with various concentrations (25–200 μg $mL^{-1}$) of Dox and Dox-$H_2Ti_3O_7$. For comparative analysis, the cells were also exposed to $H_2Ti_3O_7$ at concentrations equivalent to their respective amounts in the Dox-$H_2Ti_3O_7$ nanotubes, followed by incubation in a $CO_2$ incubator at 37 °C under 5% $CO_2$ for 24 hours. After incubation, the treatment medium was removed and replaced with fresh medium supplemented with MTT reagent (5 mg $mL^{-1}$ in PBS) and the sample was next incubated for 4 hours at 37 °C. Formazan crystals formed were dissolved in DMSO. The absorbance was recorded at 570 nm using a multimode plate reader (MPlex Pro 200, Tecan Ltd).[21]

### 2.8 The effect of Dox-loaded nanotubes on cancer cell viability, as determined using calcein AM dye

The percentage of live cells was estimated following drug-loaded nanotube treatment at 25–200 μg $mL^{-1}$, followed by cell seeding in a 96-well plate for 24 hours. The cells were rinsed with PBS twice and subsequently stained with calcein AM dye (5 μM) for 15 min. The cells were again gently rinsed with PBS to remove excess dye. The fluorescence emitted by these cells was visualized using a confocal laser scanning microscope (CLSM 880) and quantified using an imaging and multimode reader (Cytation 5 Agilent Biotek) to evaluate the impact of Dox-$H_2Ti_3O_7$ on cell viability.[22]

### 2.9 Investigation of the impact of Dox-$H_2Ti_3O_7$ on the wound closure ability of C6 cells

The effects of Dox-$H_2Ti_3O_7$ nanostructures on the migration of C6 cells were evaluated using an artificial wound-healing assay on a monolayer of C6 cells.

For comparative analysis, the cells were also exposed to $H_2Ti_3O_7$ at concentrations equivalent to their respective amounts in the Dox-$H_2Ti_3O_7$ nanotubes. This assay estimates the cellular migration and proliferation in response to a wound created on the cell layer. C6 cells were incubated for 24 hours with various treatment groups, and wound closure was monitored at intervals of 0, 6, 12, and 24 hours.[23] The area of the wound and wound closure % were quantitatively analyzed using an ImageJ plugin. The percentage of wound closure was calculated using the formula:[24]

$$\%\,\text{wound closure} = [(\text{wound area at 0 h} - \text{wound area at } x\,\text{h})/\text{wound area at 0 h}] \times 100$$

### 2.10 Intracellular and extracellular reactive oxygen species (ROS) analysis

To examine the ROS production ability of the Dox-$H_2Ti_3O_7$ nanostructures, the nanostructures were incubated with terephthalic acid (TA) at a concentration of 500 nM for 30 min. The conversion of TA to hydroxyterephthalic acid (HTA), a fluorescent compound in the presence of hydroxyl radicals, was estimated at a specific wavelength of 424 nm. The fluorescence intensity was measured using a multimode plate reader (MPlex Pro 200, Tecan Ltd).[25]

For intracellular ROS production, the cells were subjected to 100 μg $mL^{-1}$ $H_2Ti_3O_7$ nanotubes, Dox, and the Dox-$H_2Ti_3O_7$ nanotubes, followed by washing with PBS thrice. Subsequently, the cells were incubated with DCFH-DA dye at a concentration of 10 μM for 20 min, followed by washing of the cells with PBS. The intensity of fluorescence produced within the cells was estimated using an imaging and multimode reader (Cytation 5, Agilent Biotek) to assess the extent of ROS generation induced by the nanostructures.[26]

### 2.11 Comet assay for assessing DNA damage induced by Dox-$H_2Ti_3O_7$

The comet assay was performed here to investigate how Dox-$H_2Ti_3O_7$ affects DNA. The comet assay is a sensitive technique for observing DNA damage at the single-cell level.[27] In this procedure, the cells were mixed with low melting point agarose gel and placed on microscope slides. They were then treated overnight with a strong alkaline medium along with a detergent such as SDS, which breaks down the cell membranes, releasing the DNA. Following lysis, the slides were made to undergo electrophoresis under alkaline conditions, allowing damaged DNA fragments to migrate towards the anode, forming a characteristic "comet" appearance.[27] The extent of DNA damage was assessed from the DNA fragmentations observed under confocal laser scanning microscopy (CLSM-880 with AiryScan, Zeiss). This methodology enabled a comprehensive analysis of the genotoxic effects of Dox-$H_2Ti_3O_7$, contributing to our understanding of its potential implications in cellular toxicity.[28]

### 2.12 Determination of $H_2Ti_3O_7$ permeability across an *in vitro* BBB Transwell model

The ability of $H_2Ti_3O_7$ nanostructures to traverse an *in vitro* BBB model was assessed through a dual-layer setup, where the upper chamber contained bEnd.3 endothelial cells and the lower chamber housed C6 glioma cells. For this, rhodamine 6G-loaded $H_2Ti_3O_7$ nanotubes were utilized.[29] Briefly, bEnd.3 cells were cultured in the upper compartment of a Transwell plate at $5 \times 10^4$ cells per well within a 12-well plate system. The culture medium was monitored daily to maintain optimal cell health and transendothelial electrical resistance (TEER) values were measured each day to evaluate the integrity of the cell monolayer. TEER values were calculated using the formulas:

$$R(\text{tissue}) = R_{\text{total}}\ (\Omega) - R_{\text{blank}}\ (\Omega)$$

$$\text{TEER}(\text{tissue}) = M_{\text{area}}\ (\text{cm}^2)/R(\text{tissue})\ (\Omega)$$

where the area of each well was 3.5 $cm^2$ for the 12-well plates. Once TEER values exceeded 180 Ω·$cm^2$, the medium in the upper chamber was replaced with a suspension of $H_2Ti_3O_7$ nanoparticles (100 μg $mL^{-1}$) dispersed in pH 7.4 HEPES buffer. The cell monolayer was incubated at 37 °C for 24 hours to facilitate interaction. Post incubation, the absorbance of the

$H_2Ti_3O_7$-containing solution in the upper chamber ($A_u$) was measured using UV-vis spectroscopy. The permeability ratio was calculated using the formula:

$$\%\text{Transport} = (1 - A_u/A) \times 100$$

where $A_u$ represents the absorbance of the $H_2Ti_3O_7$ solution in the upper chamber after 24 hours, and $A$ denotes the initial absorbance of the $H_2Ti_3O_7$ solution prior to incubation. This methodology enabled us to assess the ability of $H_2Ti_3O_7$'s to traverse the BBB model in a quantifiable manner, providing insights into its potential for drug delivery applications targeting glioblastoma.[30]

## 3. Results and discussion

### 3.1 Physico-chemical properties of the as-grown $H_2Ti_3O_7$ nanotubes

Fig. 1a represents the FESEM image of the as-grown powder, revealing the formation of nanotubes of one-dimensional, elongated morphology with a diameter range of 15–20 nm and length in microns, as shown in the histogram presented as the lower inset of Fig. 1a. This observation matches the earlier study by Ray *et al.*[13] The crystallography phase analysis (upper inset of Fig. 1a) of the as-prepared nanostructured sample revealed the presence of diffraction lines at $2\theta$ of ~24.3° and 48.4°, matching with the (002) and (020) planes of the monoclinic crystal structure of hydrogen titanate (JCPDS card no. 41-0192). The lines indicated by 'R' match with the rutile phase of $TiO_2$ (JCPDS card no. 21-1276), which might appear due to the presence of unreacted precursor powder.

Furthermore, the detailed morphology of individual one-dimensional nanostructures was determined using high-resolution transmission electron microscopy (HRTEM) (Fig. 1b). It clearly shows that the individual nanostructures were hollow and tubular (Fig. 1b), as reported previously by Chatterjee *et al.*[31] The diameter of individual nanotubes was around 10 ± 1 nm, as represented in Fig. 1a. The lattice spacing, as seen in the inset of Fig. 1b, was calculated to be 0.3 nm, which corresponds to the (003) plane of hydrogen titanate. The EDX spectra of individual nanotubes recorded during TEM measurements also clarified the absence of any impurity in the system (Fig. 1c). The $N_2$ adsorption–desorption isotherm of the as-prepared nanotubes described the BET-specific surface area, pore volume, and average pore diameter. According to the IUPAC classification, the isotherm was typical type IV (Fig. 1d) in nature. The BET surface area was found to be 159 $m^2$ $g^{-1}$ and

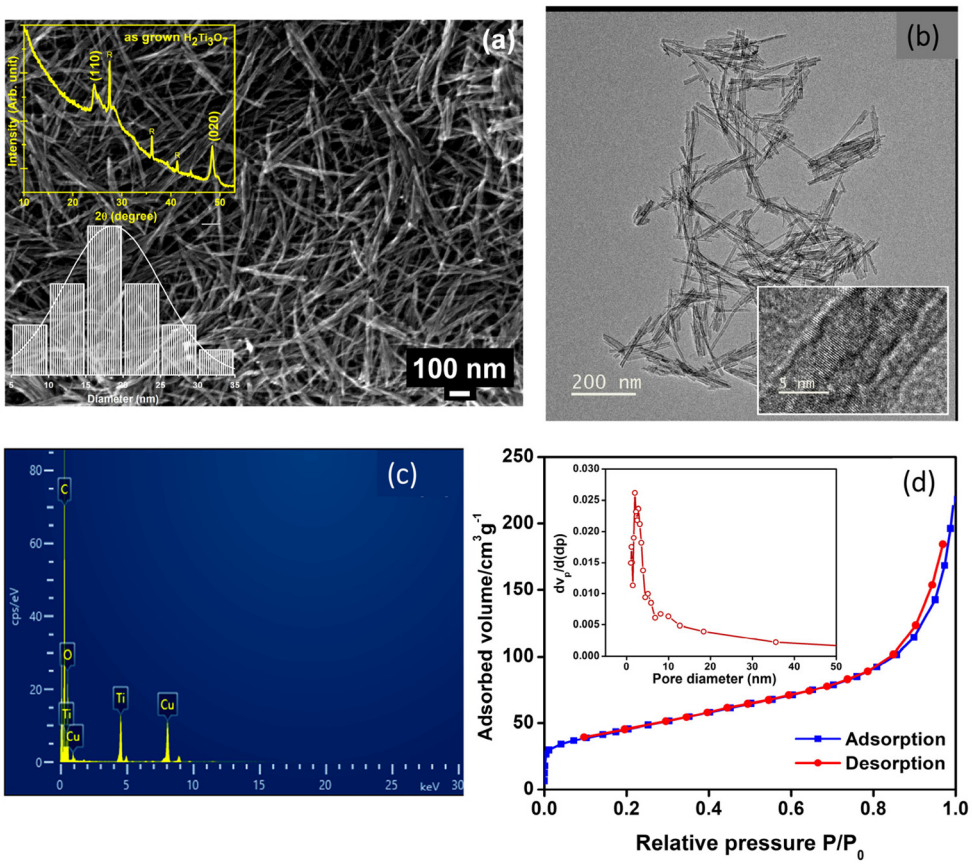


**Fig. 1** (a) Scanning electron micrograph of the as-prepared $H_2Ti_3O_7$ nanostructures, X-ray diffractogram of the same sample (upper inset), and distribution of the diameter of the nanostructures (lower inset). (b) Transmission electron micrograph of the as-prepared $H_2Ti_3O_7$ nanotubes and HRTEM image of a single nanotube (inset). (c) EDS spectrum of the same sample. and (d) Nitrogen adsorption–desorption isotherms of the as-prepared nanotubes and pore size distributions of the same sample (inset).

 

the total pore volume measured at $P/P_0$ = 0.99 was 31 $cm^3$ $g^{-1}$. The corresponding pore size distribution was calculated using the BJH method and is presented in the inset of Fig. 1d, and the average tube diameter was found to be 7.9 nm.

The large surface area and elongated morphology with a high surface-to-volume ratio of the as-prepared nanotube prompted us to check its application as a nano-carrier in drug delivery. Therefore, Dox, a model drug, was loaded onto the as-grown $H_2Ti_3O_7$ nanotubes, and the loaded nanotubes were characterized for further suitable applications.

### 3.2 Physico-chemical properties of Dox-$H_2Ti_3O_7$ nanotubes

To investigate the effect of Dox loading onto the hydrogen titanate nanotubes, FESEM and TEM were performed with the Dox-$H_2Ti_3O_7$ sample (Fig. 2). There was no distinct change in the nature and width of the particle diameter after Dox loading. The Dox-loaded nanotubes were further characterized with HRTEM, further confirming the structural integrity of the nanotubes even after Dox loading (Fig. 2b and c). The loading of Dox onto the $H_2Ti_3O_7$ nanotubes was confirmed by UV-vis absorption spectroscopy (Fig. 2d). The pristine $H_2Ti_3O_7$ nanotubes showed a strong absorption peak below 300 nm that may be corroborated by the band-edge absorption of hydrogen titanate.[6] In the case of the Dox-$H_2Ti_3O_7$ nanotubes, along with the typical band-edge absorption of $H_2Ti_3O_7$, a prominent broad peak was observed near 495 nm. This peak represents the characteristics absorption peak of Dox.[32] Loading of Dox onto the hydrogen titanate nanotubes was further confirmed by Raman spectroscopy (Fig. 2e). The Raman spectrum of the pristine $H_2Ti_3O_7$ nanotubes did not show any peak in the range of 1100 $cm^{-1}$–1900 $cm^{-1}$. In contrast, a distinct broad peak was observed in the same range in the case of the Dox-$H_2Ti_3O_7$ sample. Previously, Din *et al.* reported the presence of Dox-specific bands in this region that originate from skeletal ring vibrations (1445 $cm^{-1}$ and 1570 $cm^{-1}$) and the presence of C–O, C–O–H and C–H bonds in Dox (between 1200 $cm^{-1}$ and 1300 $cm^{-1}$).[33] The presence of such a broad peak indicated and confirmed the adsorption of doxorubicin onto the surface of $H_2Ti_3O_7$. Such a shift in the Raman peak position indicated and confirmed the adsorption and bond formation between Dox and $H_2Ti_3O_7$. The FTIR spectrum of the pure $H_2Ti_3O_7$ nanotubes showed a strong and broad O–H stretching peak at 3300 $cm^{-1}$ and an H–O–H bending peak at 1630 $cm^{-1}$ (Fig. 2f). A decrease in the intensity of these two peaks in the Dox-$H_2Ti_3O_7$ sample as compared to those of the pristine sample indicated an electrostatic interaction between the Ti–O sites at the nanotube surface and the Dox molecule that in turn possibly removed some water molecules from the surface of the nanotubes.

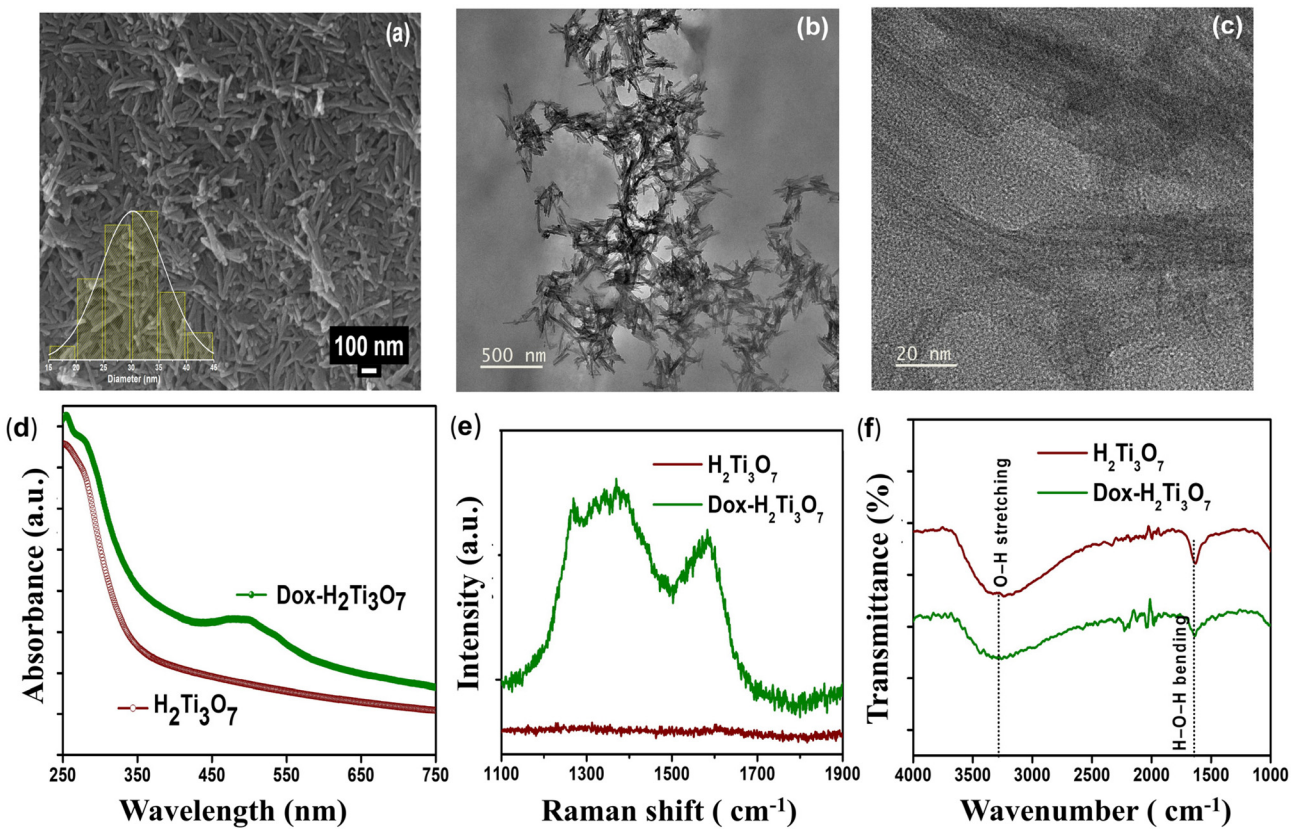


**Fig. 2** (a) Scanning electron micrograph of the Dox-$H_2Ti_3O_7$ nanostructures, the inset shows the distribution of the diameter of the nanostructures; (b) HRTEM image of the Dox-$H_2Ti_3O_7$ nanostructures; (c) high-magnification HRTEM image of the Dox-$H_2Ti_3O_7$ nanostructures that shows tubular nature even after Dox loading; (d) UV-visible spectra of the $H_2Ti_3O_7$ and Dox-$H_2Ti_3O_7$ nanotubes; (e) Raman spectra of the $H_2Ti_3O_7$ and Dox-nanotubes; and (f) FTIR spectra of the $H_2Ti_3O_7$ and Dox-$H_2Ti_3O_7$ nanotubes.

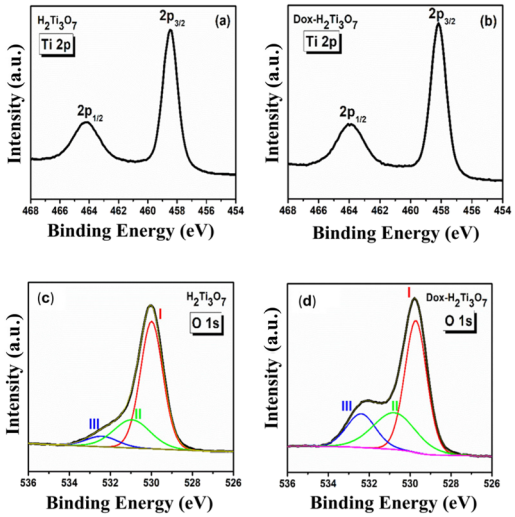


Fig. 3 XPS analysis of hydrogen titanate nanotubes. (a) and (b) Ti 2p spectra showing characteristic peaks for the $Ti^{4+}$ oxidation state; (c) and (d) O 1s spectra showing the successful drug incorporation.

X-ray photoelectron spectroscopy (XPS) is a highly sensitive technique for characterizing surface defects and chemical composition. The survey scan of the pristine $H_2Ti_3O_7$ nanotubes confirmed the presence of titanium (Ti) and oxygen (O) (Fig. S1a†). The Dox-loaded $H_2Ti_3O_7$ nanotubes showed the presence of Ti, O, and nitrogen (N) (Fig. S1b†), which confirmed the loading of Dox onto the surface of these nanotubes. Fig. 3a and b show the Ti 2p spectra of the as-grown hydrogen titanate nanotubes and doxorubicin-loaded hydrogen titanate nanotubes, respectively. Both spectra exhibited prominent peaks at approximately 458.5 eV and 464.3 eV, corresponding to Ti $2p_{3/2}$ and Ti $2p_{1/2}$, which were characteristic of the $Ti^{4+}$ oxidation state. Noteworthy changes were observed in the fine-structured O 1s spectra shown in Fig. 3c and d, indicating distinct chemical shifts associated with various oxygen environments. Deconvolution of the broad spectra using Gaussian peak fitting revealed three components centered at around 530, 531, and 533 eV. The peak at ~530 eV (denoted as I) corresponded to lattice oxygen in the hydrogen titanate matrix. The second peak, at ~531 eV (denoted as II), is attributed to oxygen deficiency,[34,35] while the third peak at ~533 eV (denoted as III) is associated with the surface hydroxyl (–OH) groups. A notable difference in the relative peak area of component III was observed between the two samples. The increased intensity of this peak in the Dox-loaded sample suggested a higher concentration of –OH moieties, confirming the successful incorporation of doxorubicin into the hydrogen titanate nanotube framework.

### 3.3 Assessment of the cellular biocompatibility of $H_2Ti_3O_7$ nanotubes

To assess the cellular biocompatibility of these nanotubes, which were to be employed as drug delivery vehicles, it is essential to evaluate their safety and compatibility within biological systems. This assessment is crucial in preventing adverse reactions, cytotoxicity, or undesirable immune responses that may arise when these nanotubes interact with living cells and tissues. This procedure involves assessing how the nanotubes interact *in vitro* in cellular models such as the L929 cell line, which is a fibroblast cell line of mouse origin, to minimize the risk of adverse outcomes and maximize their therapeutic potential.

The cells were treated with the nanotubes, and their viability and proliferation were assessed using the MTT assay, which demonstrated significant cellular viability in a concentration-dependent (25–200 μg $mL^{-1}$) manner with the nanotubes. The cell viability following incubation with the nanotubes, as depicted in Fig. 4, indicated approximately 90% viability, highlighting the use of nanotubes as a favorable option for drug delivery applications.

### 3.4 Dox loading and release kinetic studies of Dox-$H_2Ti_3O_7$ nanotubes

The loading of Dox onto the nanotubes was determined collectively with release kinetics. This contributes to the understanding of the loading and release mechanism along with the therapeutic efficacy of Dox. Dox interacted with $H_2Ti_3O_7$ nanotubes *via* hydrogen bonding, which was aided by the hydroxyl groups on the nanotube surface. These hydrogen bonding interactions play an important role in the binding mechanism between Dox and the $H_2Ti_3O_7$ nanotubes, impacting the adsorption, stability, and release kinetics of the drug from the carrier system.[32] The inclusion of hydroxyl groups on the nanotube surface increases the affinity and specificity of their interaction with Dox, improving the overall efficacy and controlling the drug release behavior for possible therapeutic uses. We observed that the loading of Dox onto the $H_2Ti_3O_7$ nanotubes reached approximately 33%, while its encapsulation percentage was around 67%.

The observed loading of Dox onto the $H_2Ti_3O_7$ nanotubes suggested the role of these nanotubes as a carrier for the drug with potential drug delivery applications, offering a promising approach for controlled release and targeted therapy in cancer treatment. The stability studies of Dox-loaded $H_2Ti_3O_7$ nanotubes were carried out in 10% FBS and PBS at pH 7.4 for 72 hours, as shown in Fig. S2.† In PBS (pH 7.4), the nanotubes appeared to maintain their structural integrity and remained well-dispersed even after 72 hours. Minimal aggregation was observed, suggesting good stability under physiological pH conditions. In FBS, these nanotubes demonstrated evidence of some aggregation compared to under the PBS conditions. This suggested that the complex protein environment of serum might have promoted some degree of particle clumping due to protein corona formation.[36]

These results suggested that the Dox-$H_2Ti_3O_7$ nanotubes exhibited reasonable stability in PBS (pH 7.4) but might be prone to aggregation in serum-containing media due to protein corona formation when exposed for longer durations. However, the overall tubular structure of the nanotubes was retained even under incubation with FBS for 72 hours.

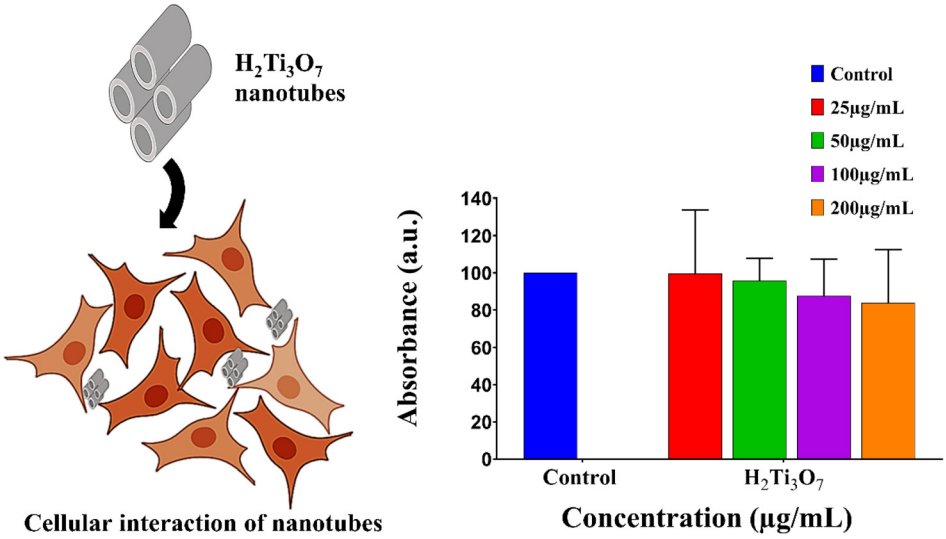


**Fig. 4** MTT assay results demonstrating the biocompatibility of $H_2Ti_3O_7$ nanotubes towards L929 cells, as the nanotubes exhibited minimal cytotoxicity and maintained cell viability above 90% after 24 hours of incubation (Created in BioRender. Choudhury, S. (2025) https://BioRender.com/k0c2v34).

The release kinetics of Dox and the Dox-$H_2Ti_3O_7$ nanotubes under physiological conditions at pH 7.4, utilizing PBS as the medium for over 24 hours, are shown in Fig. S3.† The concentration of the released drug and the drug release percentage were determined using the Dox standard curve, providing an insight into the release behavior and kinetics of Dox and the Dox-$H_2Ti_3O_7$ nanotubes in this controlled environment. The release profiles were plotted, and it was observed that whereas free Dox exhibited rapid and extensive release with approximately 70% release achieved within 72 hours, Dox-$H_2Ti_3O_7$ nanotubes demonstrated sustained release, reaching 70% release after 8 days.

This observation suggests that the nanotubes could effectively retain and release the drug in a controlled manner, enhancing its therapeutic efficacy and reducing the side effects associated with high doses of free Dox. The enhanced release profile of Dox from the $H_2Ti_3O_7$ nanotubes highlights their potential as a carrier for drug delivery applications.

### 3.5 Cellular internalization of Dox-$H_2Ti_3O_7$ nanotubes

It was previously discussed that one-dimensional nanotubes have a higher surface-to-volume ratio, which allows them more surface contacts with specific cell receptors, resulting in better targeting capabilities than zero-dimensional nanomaterials.[33] This improved targeting ability allows for the selective accumulation of these nanoparticles at the appropriate spot, increasing their cellular uptake and efficacy.

The results showed an increased fluorescence intensity in the case of the Dox-$H_2Ti_3O_7$ nanotubes, indicating a more efficient uptake of the nanotubes by the cells. The uptake of the nanotubes was further confirmed by staining the nucleus of the cells with DAPI, a fluorescent dye that binds to DNA. In the case of cells treated with only Dox or the $H_2Ti_3O_7$ nanotubes, the intensity of DAPI staining was found to be high, indicating the presence of intact nuclei. However, in the case of cells treated with the Dox-$H_2Ti_3O_7$ nanotubes, the intensity of DAPI staining was significantly reduced, suggesting Dox-induced DNA damage as previously reported by Müller *et al.*,[37] leading to cell death and morphological changes, as shown in Fig. 5. As per sources in the literature, $TiO_2$ NPs demonstrate pH-responsive drug release (80% at pH 6.5 *vs.* 20% at pH 7.4),[38] which aligns with the potential of $H_2Ti_3O_7$ nanotubes for glioma-specific delivery. The nanotube structure enhanced the drug-loading capacity and enacted controlled release, and helped in improving drug delivery in acidic tumor microenvironments.[39] Hence, these results suggest that the $H_2Ti_3O_7$ nanotubes could effectively deliver an increased amount of Dox to the cancer cellular environment, resulting in enhanced anticancer activity.

### 3.6 *In vitro* anticancer evaluation of Dox-$H_2Ti_3O_7$ nanotubes

The anticancer properties of the Dox-$H_2Ti_3O_7$ nanotubes were evaluated by measuring the cell viability of the treated C6 cancer cells. The MTT assay, a widely used technique, was employed to quantify the metabolic activity of the cells as an indicator of their viability.

The results from the MTT assay provided valuable insights into the potential of the $H_2Ti_3O_7$ nanotubes as a biocompatible carrier for delivering Dox to cancer cells. The Dox-$H_2Ti_3O_7$ nanotubes displayed a controlled release profile of the drug, leading to the exhibition of targeted therapeutic behavior, and only around 30% viable cancer cells were observed at a concentration of 200 μg $mL^{-1}$ after an incubation period of 24 hours. This was in contrast to the treatment with free Dox, which resulted in a 20% lower cytotoxic effect on the cells in comparison with the Dox-$H_2Ti_3O_7$ nanotubes at a similar concentration, as shown in Fig. 6. The controlled release and targeted delivery of Dox achieved through the $H_2Ti_3O_7$ nanotubes led to

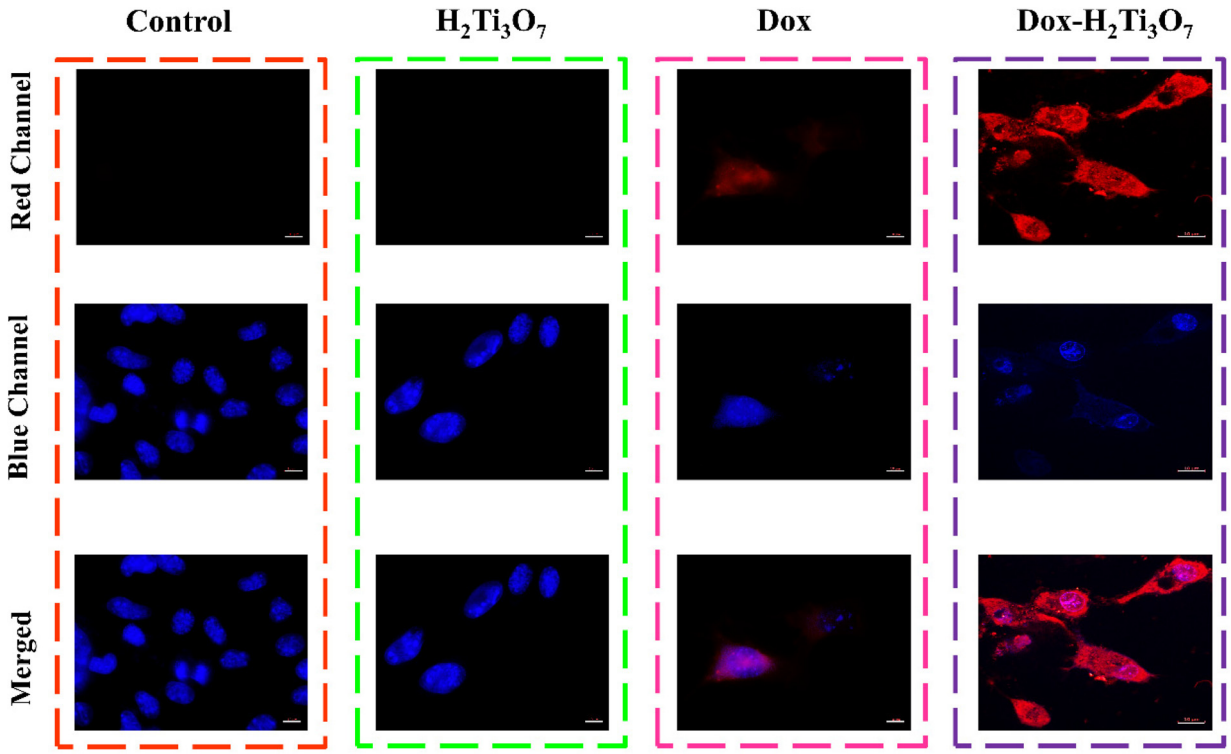


**Fig. 5** Investigation of the *in vitro* cellular uptake of the Dox-loaded $H_2Ti_3O_7$ nanotubes in C6 cells. The delivery of Dox to the glioma cells and subsequent release of the drug within the cells were monitored using confocal laser scanning microscopy (scale bar: 10 μm).

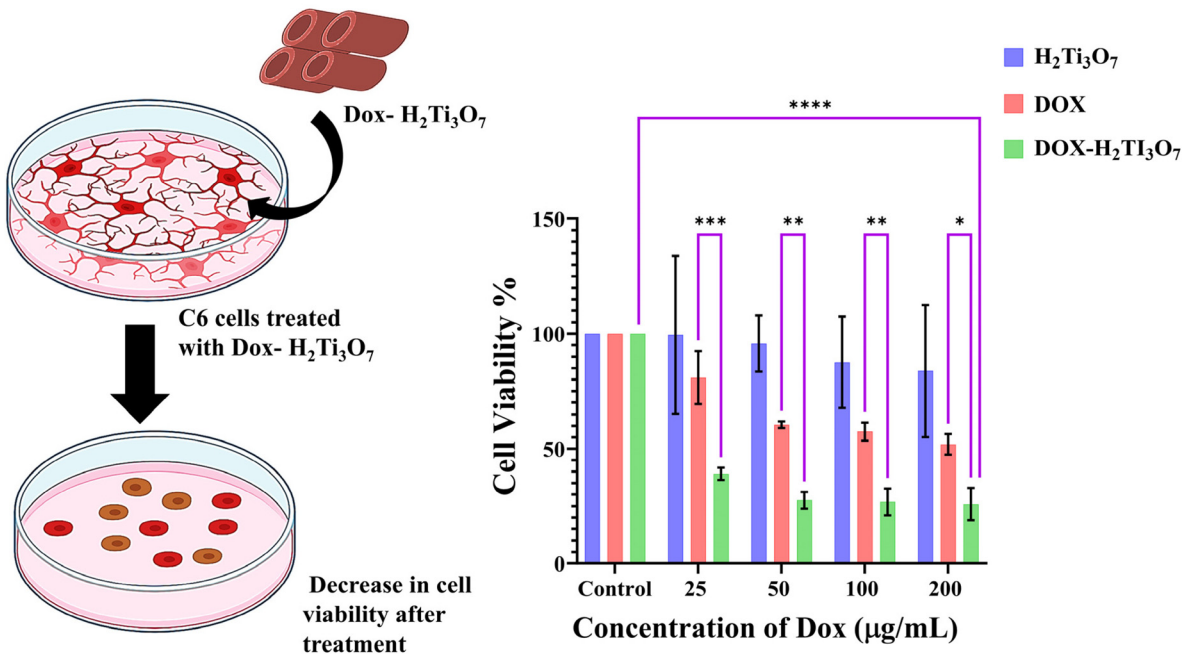


**Fig. 6** Enhanced anticancer efficacy of the Dox-$H_2Ti_3O_7$ nanotubes, demonstrating through controlled drug release and targeted therapeutic action against glioma cells. Cell viability analysis *via* the MTT assay highlighting the potential of these nanotubes as a biocompatible drug delivery system. The data are depicted in a bar graph illustrating the cell viability percentage. The samples were taken at equivalent Dox concentrations based on the amount of drug loaded on the nanotubes. Subsequently, a two-way ANOVA analysis, followed by Dunnett's test was utilized to evaluate the statistical significance between the control groups and the treated samples. The results were reported as the mean ± SD with significance levels denoted by $*p < 0.05$ and $**p < 0.01$ (Created in BioRender. Choudhury, S. (2025) https://BioRender.com/yq43mhu).

enhanced anticancer activities compared to the free drug. The tubular morphology (~100–200 nm) of the $H_2Ti_3O_7$ nanotubes may favor prolonged circulation and tumor targeting *via* the enhanced permeability and retention (EPR) effect, similar to that of carbon nanotubes.[40] These one-dimensional $H_2Ti_3O_7$ nanotubes exhibit superior drug-loading capacities attributed to their increased surface-to-volume ratio. Their expanded surface area allows for more efficient drug encapsulation and delivery, enhancing the therapeutic potential of these nanotubes. The unique structural characteristics of one-dimensional nanotubes offer a promising platform for optimizing drug loading efficiency and efficacy, paving the way for advanced drug delivery systems with enhanced performance and targeted delivery capabilities.

### 3.7 Assessing cell viability with calcein AM dye

To investigate the reduction in cell viability induced by the Dox-$H_2Ti_3O_7$ nanotubes, the cells were exposed to optimized concentrations of the nanostructures, ranging from 25 to 200 μg $mL^{-1}$. Following this treatment, the cells were stained with calcein AM dye for 15 minutes. This fluorescent dye is a valuable tool for assessing cell viability, as it is taken up by live cells and then enzymatically cleaved by esterases within the cells to produce highly fluorescent calcein. The calcein molecule is retained within viable cells, allowing for the visualization of the number of living cells in the sample.

Here in, the control cells exhibited a strong green fluorescence, indicating a high number of viable cells. In contrast, the cells treated with the Dox-$H_2Ti_3O_7$ nanotubes and those treated with free Dox displayed a significant decrease in green fluorescence intensity. This reduction in fluorescence intensity is a direct indicator of the decrease in cellular viability, suggesting that the treatment with the Dox-$H_2Ti_3O_7$ nanotubes and free Dox resulted in a concentration-dependent reduction in the number of viable cells, as shown in Fig. 7a and b. The cells were also treated with $H_2Ti_3O_7$ nanotubes and they demonstrated a similar green fluorescence intensity to that of the control cells, confirming their viability in the presence of the carrier (Fig. S4†). Thus, we can conclude from our results that the nanotubes can serve as an effective drug delivery system, potentially improving the therapeutic efficacy and reducing the side effects associated with the direct administration of Dox.

### 3.8 Evaluation of the wound closure rate and cellular migration characteristics

The wound closure assay was performed on C6 cells that were subjected to various treatment groups. In this experiment, a wound was created on a confluent monolayer of C6 cells using a microtip. The cells were then incubated with different treatment groups for 24 hours at two concentrations: 50 μg $mL^{-1}$ and 100 μg $mL^{-1}$.

Microscopic imaging of the wound area was conducted at regular intervals at 0, 6, 12, and 24 hours to evaluate the dynamics of wound closure. At the initial time point (0 hours), all treatment groups exhibited similar wound areas.

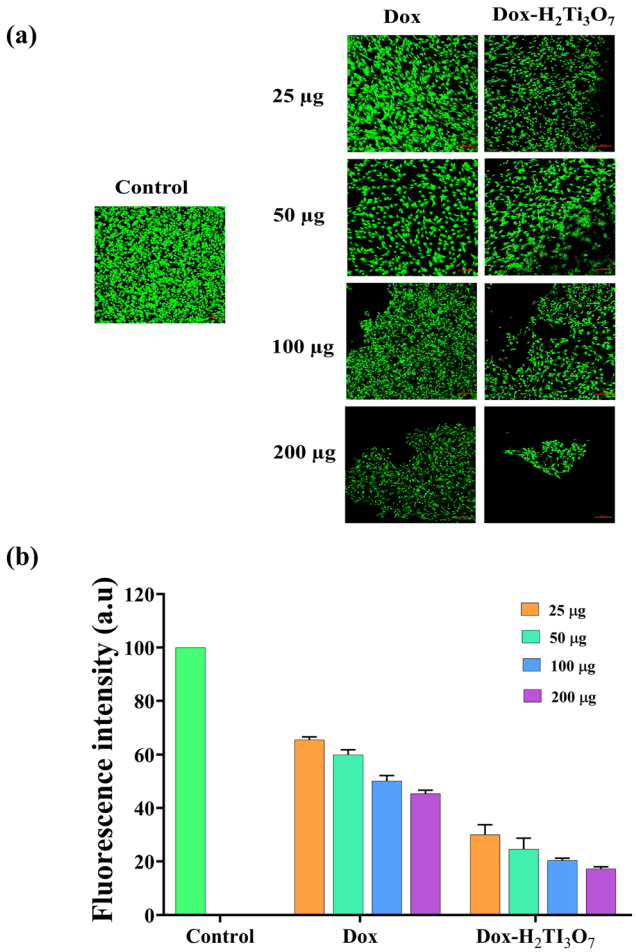


**Fig. 7** Impact of the Dox-$H_2Ti_3O_7$ nanotubes on the viability of C6 cells as visualized through calcein AM staining. (a) A qualitative assessment of the decrease in fluorescence intensity observed in cells treated with control in comparison with those treated with the Dox and Dox-$H_2Ti_3O_7$ nanotubes. (b) Concentration-dependent decrease in fluorescence intensity in the cells treated with Dox and Dox-$H_2Ti_3O_7$ nanotubes in comparison with the untreated cells and the biocompatible $H_2Ti_3O_7$ nanotubes. This was demonstrated through a bar graph representation of the data (scale bar: 100 μm). The samples were taken at equivalent Dox concentrations based on the amount of drug loaded on the nanotubes.

A significant reduction in the wound area was observed across all groups after 24 hours. Notably, both the control group and the $H_2Ti_3O_7$ treatment group demonstrated nearly complete wound closure, achieving percentages close to 100%, which indicated strong healing capabilities under these treatment conditions. In contrast, the groups treated with Dox and Dox-$H_2Ti_3O_7$ showed considerably lower percentages of wound closure, with values of around 30% at the highest concentration (100 μg $mL^{-1}$), as illustrated in Fig. 8a and b.

The findings drawn from the wound closure assay results indicated that the treatment of C6 cells with Dox-$H_2Ti_3O_7$ significantly impaired cell migration and wound healing compared to the control and $H_2Ti_3O_7$ groups. This suggests that the presence of Dox in the drug-loaded carrier system nega-

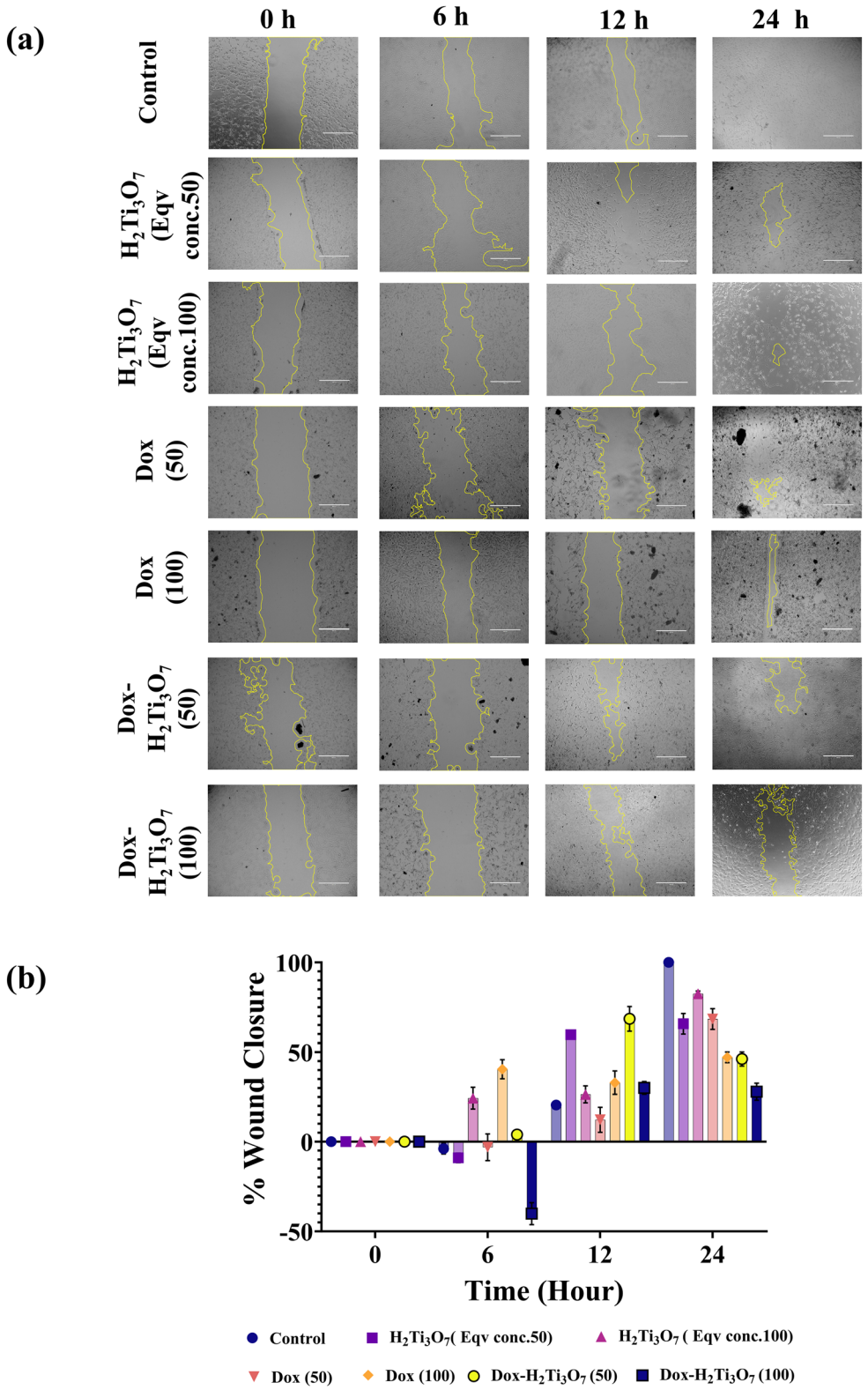


**Fig. 8** Wound closure assay results demonstrating the effects of various treatment groups on C6 cell migration. (a) Microscopic images captured at 0-, 6-, 12-, and 24 hours post-treatment. (b) Percentage of wound closure quantified at various time points, revealing nearly complete closure in the control and $H_2Ti_3O_7$ groups, while Dox and Dox-$H_2Ti_3O_7$ groups showed significantly reduced closure rates. The samples were taken at equivalent Dox concentrations based on the amount of drug loaded on the nanotubes.

tively affected the migratory capacity of cancer cells, potentially due to its cytotoxic effects.

### 3.9 Estimating reactive oxygen species (ROS) production

Dox is recognized for its ability to generate ROS through various pathways, leading to the production of highly reactive hydroxyl radicals.[41] TA was employed as a fluorescent probe to quantify the generation of hydroxyl radicals by the Dox-$H_2Ti_3O_7$ nanotubes. Upon incubation with these nanostructures, TA reacts with the produced hydroxyl radicals, leading to the formation of a product, HTA. The HTA emits a fluorescence signal at a specific wavelength of 424 nm, which was utilized to estimate the production of hydroxyl radicals by the Dox-$H_2Ti_3O_7$ nanotubes, as shown in Fig. 9a. The potential of these nanotubes in generating reactive oxygen species was also estimated in the intracellular environment. DCFH-DA was utilized to detect the ROS produced in the cells. The compound is sensitive to oxidation, and in the presence of intracellular ROS, DCFH-DA is metabolically oxidized to fluorescent DCF in the cells.[42] The fluorescence intensity generated by the cells at a treatment concentration of 100 μg $mL^{-1}$ was determined. It was noted that when the cells were incubated with the Dox-$H_2Ti_3O_7$ nanotubes, an increased fluorescence intensity was observed throughout the samples in comparison with other treatment groups, establishing that a higher amount of ROS is being produced in the cells treated with the Dox-$H_2Ti_3O_7$ nanotubes, as shown in Fig. 9b.

### 3.10 Assessment of DNA damage using the comet assay

The analysis of DNA damage in C6 cells treated with various treatment groups at a concentration of 100 μg $mL^{-1}$ revealed significant findings. Notably, the formation of visible comets was observed in the cells treated with Dox and the Dox-$H_2Ti_3O_7$ nanotubes, indicating the presence of DNA strand breaks. To quantify this damage, we employed the CometScore application to evaluate the comet tail length and the percentage of tail DNA. Utilizing the images captured through confocal microscopy, we accurately measured these parameters, which are critical indicators of DNA integrity.

As illustrated in Fig. 10a, cellular changes were documented following treatment with different groups, followed by DNA extraction in a highly alkaline medium and subsequent electrophoresis to visualize comet formation. Fig. 10b and c present the quantified tail length and percentage of tail DNA for each treatment group post-electrophoresis. In total, 20 comets were analyzed for each group, and the data were graphically presented to facilitate comparison. The results indicated that the cells treated with the Dox-$H_2Ti_3O_7$ nanotubes exhibited a significantly greater tail length and a higher percentage of tail DNA compared to that in the other treatment groups. This suggests that exposure to Dox-$H_2Ti_3O_7$ led to increased DNA damage, highlighting its potential genotoxic effects on C6 cells.

### 3.11 Assessment of $H_2Ti_3O_7$ permeability using an *in vitro* BBB Transwell model

The BBB is a highly selective and semipermeable membrane that serves as a critical protective barrier between the bloodstream and the central nervous system (CNS). Composed of tightly packed endothelial cells, its selective permeability is crucial for maintaining the brain's microenvironment.[43] However, its restrictive nature poses significant challenges for drug delivery in treating CNS disorders, as various therapeutic

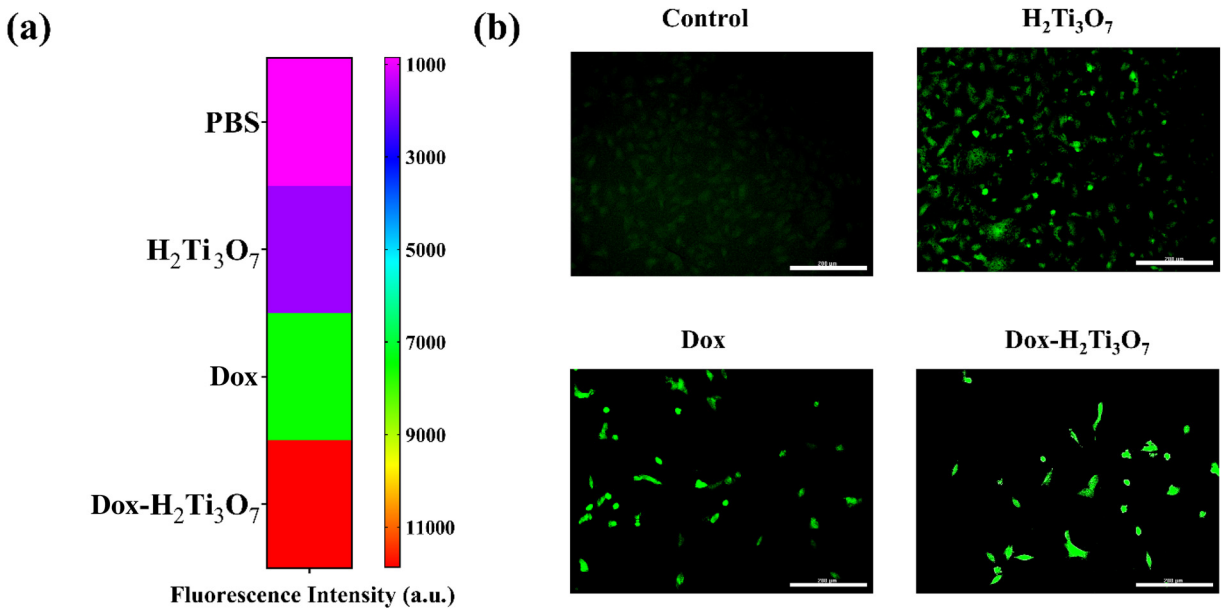


**Fig. 9** Comparative analysis of TA and DCFH-DA assays providing a comprehensive understanding of ROS detection and quantification. (a) Graphical representation of a heat map demonstrating the quantified fluorescence intensity produced by the TA assay, which specifically targets the hydroxyl radicals (•OH). (b) DCFH-DA assay reports qualitatively detecting intracellular ROS produced by the cells treated with free Dox and Dox-$H_2Ti_3O_7$ nanotubes (scale bar: 200 μm).

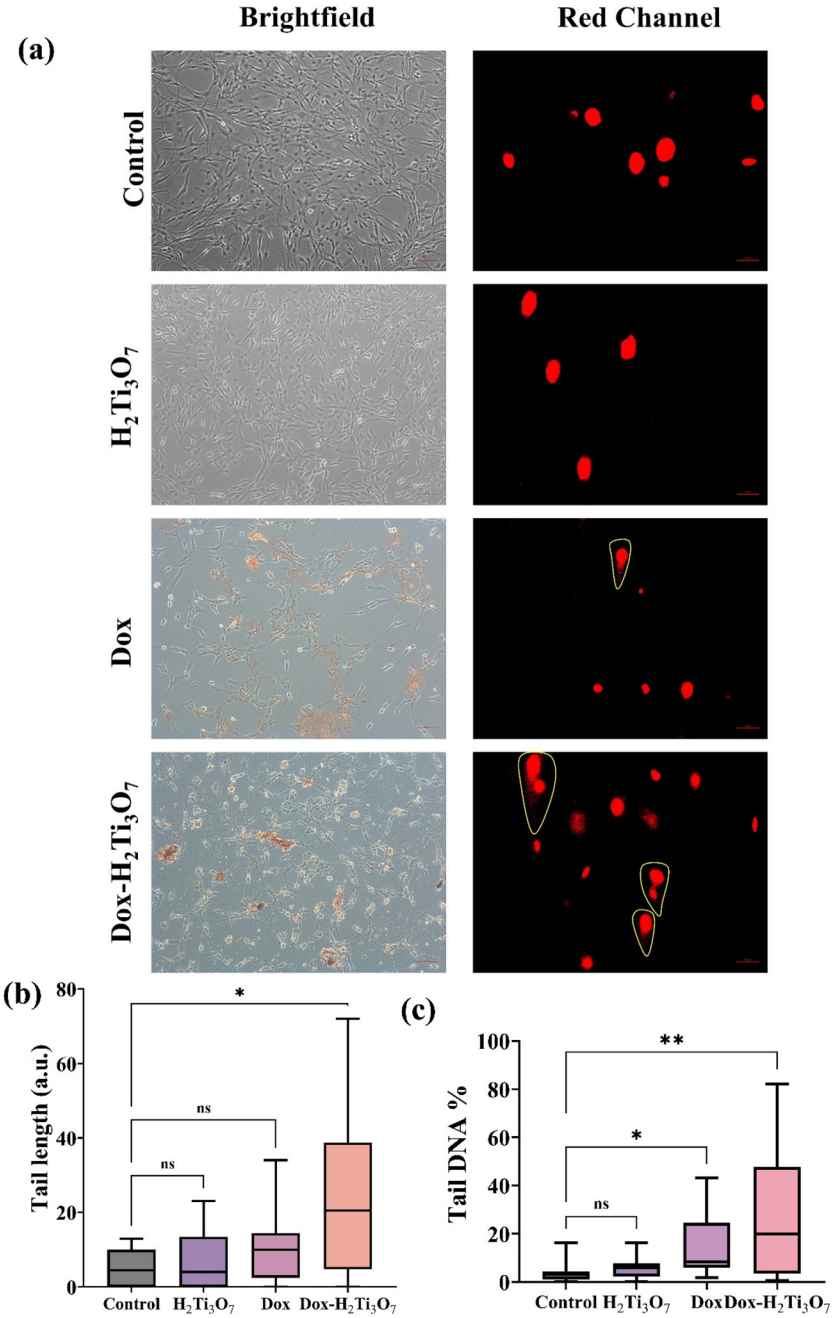


**Fig. 10** Assessment of DNA damage in C6 cells treated with various treatment groups analyzed using the comet assay. (a) Confocal microscopic images illustrating cellular changes post-treatment followed by DNA comet formation. (b) Quantification of the comet tail length for each treatment group, indicating the extent of DNA damage. (c) Percentage of tail DNA observed after electrophoresis, demonstrating the level of DNA fragmentation (scale bar: 100 μm for the brightfield images and 10 μm for the fluorescence images).

modalities struggle to cross this barrier effectively. Therefore, an effective drug carrier must be capable of penetrating the BBB to deliver therapeutic agents specifically to glioma cells.

Hence, the successful traversal of the BBB by nanotubes was simulated using a Transwell system, where bEnd.3 cells served as a model for assessing cellular permeability.[44] This approach not only mimics physiological conditions but also provides a controlled environment to study the interaction between drug carriers and the BBB.[45] To evaluate the permeability characteristics of the $H_2Ti_3O_7$ nanotubes, we conducted a qualitative and quantitative analysis by loading them with rhodamine 6G dye. In this setup, the Transwell apparatus consisted of a 0.4 μm insert in a 12-well plate, allowing for the measurement of TEER as an indicator of barrier integrity. Once the TEER value exceeded 180 Ω·cm$^2$, the upper chamber was replaced with the $H_2Ti_3O_7$ nanotubes dispersed in HEPES buffer (pH 7.4). The nanotubes were then incubated in the chamber for 24 hours to evaluate their ability to cross the

 

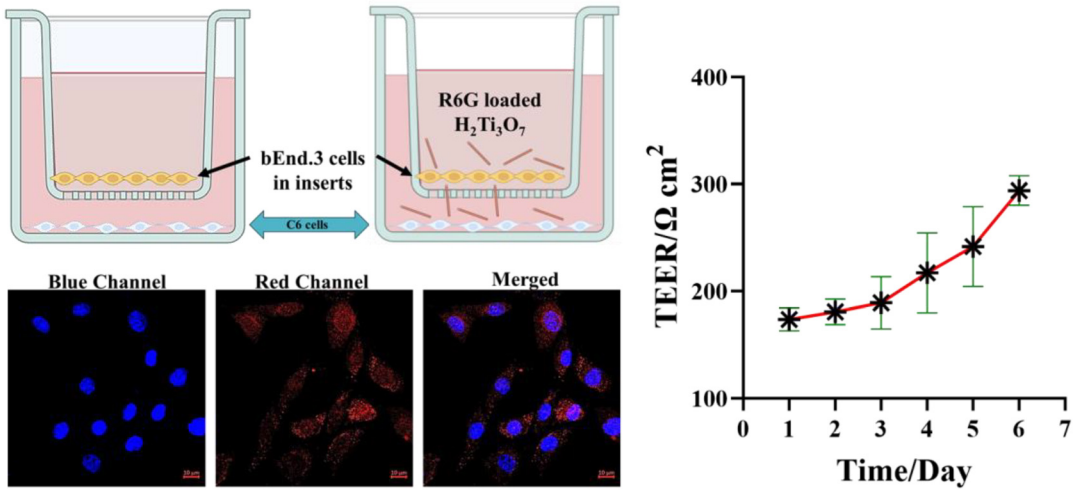


**Fig. 11** Schematic representation of the TEER calculation method, illustrating the rhodamine 6G-loaded nanotubes as they traverse the bEnd.3 cell layer and enter C6 cells, supported by confocal microscopic images that confirm their successful uptake. TEER values were obtained over a 7-day period (scale bar: 10 μm) (Created in BioRender. Choudhury, S. (2025) https://BioRender.com/q43mvxr).

endothelial layer and reach the lower chamber containing C6 glioma cells. We also performed confocal microscopy, where we observed red fluorescence in the cells, indicating that the rhodamine 6G-loaded nanotubes successfully traversed the bEnd.3 endothelial cell layer and were subsequently taken up by C6 cells, as shown in Fig. 11. The potential mechanism of BBB permeabilization by the $H_2Ti_3O_7$ nanotubes was inferred from the Transwell BBB model studies conducted in Fig. 11. Studies on titanium dioxide ($TiO_2$) nanoparticles suggest that the size and shape critically influence BBB permeabilization, with smaller spherical particles (<50 nm) exhibiting superior diffusion.[46,47] The $H_2Ti_3O_7$ nanotubes are slender rods with an approximate diameter of 15–20 nm and their elongated structure could facilitate localized membrane interactions, promoting cytoskeletal reorganization (*e.g.*, F-actin stress fiber formation) and transient paracellular gap formation, as seen in $TiO_2$-NP studies.[46] These findings align with those of broader nanocarrier research, where tailored geometries (*e.g.*, nanotubes and nanorods) are optimized for BBB traversal,[47] suggesting that the $H_2Ti_3O_7$ nanotubes might exploit passive paracellular leakage for permeabilization of the BBB.

After 24 hours of incubation, the permeability ratio (%) of $H_2Ti_3O_7$ was calculated using UV-vis spectrophotometry. The permeability ratio was determined to be 28.05% using the equation mentioned in section 2.12. This finding highlights the potential of the $H_2Ti_3O_7$ nanotubes as effective carriers for drug delivery across the BBB. The ability of these nanotubes to penetrate the BBB and deliver therapeutic agents directly to tumor cells could significantly enhance the treatment efficacy for brain tumors.

## 4. Conclusion

The findings from this investigation underscore the significant potential of $H_2Ti_3O_7$ nanotubes as a biocompatible and effective drug delivery system in cancer therapy. The encapsulation of the chemotherapeutic agent Dox into $H_2Ti_3O_7$ nanotubes demonstrated an impressive drug loading capacity of approximately 33%, with an encapsulation efficiency reaching up to 67%. These results indicate that the $H_2Ti_3O_7$ nanotubes can serve as excellent platforms for the targeted delivery of anticancer drugs, potentially enhancing therapeutic efficacy while minimizing off-target effects. The controlled-release kinetics associated with these nanotubes results in better treatment outcomes and reduced side effects in cancer patients.

In addition to their drug delivery capabilities, *in vitro* studies revealed a concentration-dependent reduction in cell viability when the Dox-$H_2Ti_3O_7$ nanotubes were incubated with cancer cells, suggesting their effectiveness in inducing cytotoxicity and inhibiting tumor cell growth. The assessment of ROS generation using the TA and DCFH-DA assays further elucidated the mechanisms by which Dox-$H_2Ti_3O_7$ enhances anticancer activity, as increased ROS production, particularly hydroxyl radicals, contributes to the cytotoxic effects of these nanoparticles.

Furthermore, the wound healing study demonstrated that while $H_2Ti_3O_7$ facilitated significant wound closure, the presence of Dox in the drug-loaded nanotubes notably impaired cell migration, with wound closure percentages significantly lower than those observed in the control groups. This dual analysis of wound healing and DNA damage *via* the comet assay highlighted that treatment with Dox-$H_2Ti_3O_7$ resulted in increased DNA damage, as evidenced by greater comet tail lengths and higher percentages of tail DNA compared to other treatment groups.

The $H_2Ti_3O_7$ nanotubes demonstrated a permeability ratio of 28.05% across the BBB model, indicating their potential as effective drug carriers. Additionally, the successful uptake of rhodamine 6G-loaded nanotubes by C6 glioma cells suggests that these nanotubes could be promising candidates for targeted therapeutic delivery in treating brain tumors.

While our study primarily explores the fundamental properties and potential of the $H_2Ti_3O_7$ nanotubes for glioma therapy, significant future work in this direction is suggested to address these important factors. Regarding scalability, we believe that the $H_2Ti_3O_7$ nanotubes can be effectively upscaled due to the cost-effectiveness of the raw materials required for their production. This economic feasibility is a significant advantage in moving towards large-scale manufacturing. Additionally, the drug used in our study, Dox, is already widely utilized in clinical settings for treating various types of cancer.

Overall, these findings illustrate that the nanotubes offer a promising strategy for effective drug delivery and possess multifunctional properties that enhance their permeability and anticancer potential. The ability to efficiently load and release chemotherapeutic agents while generating ROS further demonstrates the versatility of this one-dimensional nanoparticle system. Continued exploration through further *in vitro* and *in vivo* studies is essential to fully elucidate the therapeutic efficacy and safety profile of Dox-loaded $H_2Ti_3O_7$ nanotubes as a novel nanomedicine for cancer treatment.

## Author contributions

Samraggi Choudhury: conceptualization, data curation, formal analysis, investigation, methodology, project administration, and writing – original draft. Ghrutanjali Sahu: data curation, formal analysis, and writing – original draft. Pankaj Kharra: investigation, methodology, and project administration. Himanshu Sekhar Panda: investigation, project administration, and validation. Laxmidhar Besra: formal analysis. Sriparna Chatterje: investigation, methodology, project administration, resources, software, supervision, validation, visualization, writing – original draft, and writing – review & editing. Jiban Jyoti Panda: funding acquisition, conceptualization, investigation, methodology, project administration, formal analysis, resources, software, supervision, validation, visualization, writing – original draft, and writing – review & editing.

## Data availability

All data are available in the Results section and the ESI† of the manuscript and no additional source data are required.

## Conflicts of interest

The authors declare that they have no known competing financial interests or personal relationships that could have appeared to influence the work reported in this paper.

## Acknowledgements

The authors express gratitude for the support provided by INST; they acknowledge the ICMR extramural grant (EMDR-2023-0000790), the SERB-POWER grant from the Department of Science and Technology (DST) India (SPG/2021/002910), the Council of Scientific and Industrial Research (CSIR) India grant (37/1755/23/EMR-II), and the Department of Biotechnology (DBT) India grant (BT/PR36632/NNT/28/1694/2020 and BT/13/IYBA/2020/08).

The authors acknowledge the Central Characterization Cell of CSIR-IMMT for characterization support. The Director, CSIR-IMMT is acknowledged for his consistent support and encouragement. The authors also acknowledge the financial support from CSIR-India (13(9205-A)/2021-POOL). Authors also acknowledge the support from Biorender.com for the creation of figures in the manuscript.

## References

1 J. Shin, N. Kang, B. Kim, H. Hong, L. Yu, J. Kim, H. Kang and J. S. Kim, *Chem. Soc. Rev.*, 2023, **52**, 4488–4514.
2 B. S. Chhikara, B. Rathi and K. Parang, *J. Mater. Nanosci.*, 2019, 47–66.
3 J. Kaur, G. S. Gill and K. Jeet, *Nanosci. Nanotechnol. Drug Delivery*, 2018, 113–135.
4 Z. Liu, J. T. Robinson, S. M. Tabakman, K. Yang and H. Dai, *Mater. Today*, 2011, **14**, 316–323.
5 T. Kasuga, M. Hiramatsu, A. Hoson, T. Sekino and K. Niihara, *Langmuir*, 1998, **14**, 3160–3163.
6 S. Chatterjee, K. Bhattacharyya, P. Ayyub and A. K. Tyagi, *J. Phys. Chem. C*, 2010, **114**, 9424–9430.
7 F. Pignanelli, L. Fernández-Werner, M. Romero, D. Mombrú, M. A. Tumelero, A. A. Pasa, E. Germán, R. Faccio and Á. W. Mombrú, *Mater. Res. Bull.*, 2018, **106**, 40–48.
8 I. Chakraborty, S. Chatterjee and P. Ayyub, *Appl. Phys. Lett.*, 2011, 99.
9 R. Chakraborty, B. Sen, S. Chatterjee and P. Chattopadhyay, *Radiochim. Acta*, 2013, **101**, 33–36.
10 J. Yang, L. Lian, P. Xiong and M. Wei, *Chem. Commun.*, 2014, **50**, 5973–5975.
11 J. Li, Z. Tang and Z. Zhang, *Chem. Mater.*, 2005, **17**, 5848–5855.
12 S. Sim, E. B. Cho and S. Chatterjee, *Chem. Eng. J.*, 2016, **303**, 64–72.
13 M. Ray, S. Chatterjee, T. Das, S. Bhattacharyya, P. Ayyub and S. Mazumdar, *Nanotechnology*, 2011, 22.
14 Y. Ranjous, G. Regdon, K. Pintye-Hódi and T. Sovány, *Drug Discovery Today*, 2019, **24**, 1704–1709.
15 S. Dhal, P. Das, M. K. Rajbhar, S. Chatterjee, W. Möller, S. Chatterjee and N. Ramgir, *J. Mater. Chem. C*, 2018, **6**, 1951–1958.
16 G. A. M. Mersal, N. Y. Mostafa and A. E. H. Omar, *Mater. Res. Express*, 2017, **4**, 085031.
17 S. Naderinezhad, G. Amoabediny and F. Haghiralsadat, *RSC Adv.*, 2017, **7**, 30008–30019.
18 O. Tacar, P. Sriamornsak and C. R. Dass, *J. Pharm. Pharmacol.*, 2013, **65**, 157–170.

 

19 M. Kciuk, A. Gielecińska, S. Mujwar, D. Kołat, Ż. Kałuzińska-Kołat, I. Celik and R. Kontek, *Cells*, 2023, **12**, 659.
20 S. Voruganti, J.-J. Qin, S. Sarkar, S. Nag, I. A. Walbi, S. Wang, Y. Zhao, W. Wang and R. Zhang, *Oncotarget*, 2015, **6**(25), 21379.
21 S. Chibh, A. Kour, N. Yadav, P. Kumar, P. Yadav, V. S. Chauhan and J. J. Panda, *ACS Omega*, 2020, **5**, 3365–3375.
22 P. Decherchi, P. Cochard and P. Gauthier, *J. Neurosci. Methods*, 1997, **71**(2), 205–213.
23 S. Azzam, L. Tomasova, C. Danner, M. Skiba, M. Klein, Z. Guttenberg, S. Michaelis and J. Wegener, *Sci. Rep.*, 2024, **14**(1), 9103.
24 A. Suarez-Arnedo, F. T. Figueroa, C. Clavijo, P. Arbeláez, J. C. Cruz and C. Muñoz-Camargo, *PLoS One*, 2020, **15**(7), e0232565.
25 J. Čapek and T. Roušar, *Molecules*, 2021, **26**, 4710.
26 M. Sharma, S. Choudhury, A. Babu, V. Gupta, D. Sengupta, S. A. Ali, M. D. Dhokne, A. K. Datusalia, D. Mandal and J. J. Panda, *Biomater. Sci.*, 2024, 1801–1821.
27 A. R. Collins, *Mol. Biotechnol.*, 2004, **26**, 4710.
28 P. L. Olive and J. P. Banáth, *Nat. Protoc.*, 2006, **1**, 23–29.
29 S. Shityakov, E. Salvador, G. Pastorin and C. Förster, *Int. J. Nanomed.*, 2015, **10**, 1703–1713.
30 N. Aggarwal, G. Singh, H. S. Panda and J. J. Panda, *J. Mater. Chem. B*, 2024, **12**(4), 10665–10681.
31 S. Chatterjee, S. Bhattacharyya, D. Khushalani and P. Ayyub, *Cryst. Growth Des.*, 2010, **10**, 1215–1220.
32 A. Biswas and C. Prathibha, *Mater. Adv.*, 2022, **3**, 5947–5963.
33 F. U. Din, W. Aman, I. Ullah, O. S. Qureshi, O. Mustapha, S. Shafique and A. Zeb, *Int. J. Nanomed.*, 2017, **12**, 7291–7309.
34 P. Das, S. Das, S. Ratha, B. Chakraborty and S. Chatterjee, *Electrochim. Acta*, 2021, **371**, 137774.
35 P. P. Das, S. A. Agarkar, S. Mukhopadhyay, U. Manju, S. B. Ogale and P. S. Devi, *Inorg. Chem.*, 2014, **53**(8), 3961–3972.
36 C. Corbo, R. Molinaro, A. Parodi, N. E. Toledano Furman, F. Salvatore and E. Tasciotti, *Nanomedicine*, 2016, **11**, 81–100.
37 I. Müller, D. Niethammer and G. Bruchelt, *Int. J. Mol. Med.*, 1998, **1**, 491–495.
38 T. López, S. Recillas, P. Guevara, J. Sotelo, M. Alvarez and J. A. Odriozola, *Acta Biomater.*, 2008, **4**(6), 2037–2044.
39 M. I. Al-Shemri, M. Aliannezhadi, R. A. Ghaleb and M. J. Al-Awady, *Sci. Rep.*, 2024, **14**(1), 25998.
40 J. Pulit-Prociak, O. Długosz, A. Staroń, D. Domagała, K. Pociecha, M. Grabowski, M. Zielina and M. Banach, *ACS Omega*, 2024, **9**(34), 36220–33623.
41 D. Cappetta, A. De Angelis, L. Sapio, L. Prezioso, M. Illiano, F. Quaini, F. Rossi, L. Berrino, S. Naviglio and K. Urbanek, *Oxid. Med. Cell. Longevity*, 2017, 1521020.
42 N. Ruijter, M. van der Zee, A. Katsumiti, M. Boyles, F. R. Cassee and H. Braakhuis, *NanoImpact*, 2024, **35**, 100521.
43 D. Wu, Q. Chen, X. Chen, F. Han, Z. Chen and Y. Wang, *Signal Transduction Targeted Ther.*, 2023, 8.
44 I. Noorani and J. de la Rosa, *Nat. Commun.*, 2023, 14.
45 S. Zha, H. Liu, H. Li, H. Li, K. L. Wong and A. H. All, *ACS Nano*, 2024, **18**, 1820–1845.
46 X. Liu, B. Sui and J. Sun, *J. Mater. Chem. B*, 2017, **5**(48), 9558–9570.
47 G. Sierri, I. Saenz-De-Santa-Maria, A. Renda, M. Koch, P. Sommi, U. Anselmi-Tamburini, M. Mauri, A. D'Aloia, M. Ceriani, D. Salerno, F. Mantegazza, C. Zurzolo and F. Re, *Nanoscale*, 2025, **17**(2), 992–1006.